RESEARCH

Open Access

Hybrid control using fuzzy logic and adaptive space vector modulation for reduction of torque ripples in PM-BLDC motor drive

Vijay Kumar Karan[1*], Aftab Alam[1] and Amarnath Thakur[2]

*Correspondence:
vijaykaran1952@gmail.com

[1] Department of Electrical &
Electronics Engineering, Birla
Institute of Technology, Mesra,
Ranchi, India
[2] Department of Electrical
Engineering, National Institute
of Technology, Jamshedpur, India

Abstract

A novel hybrid control strategy for reducing torque ripple in permanent magnet brushless direct current motors has been developed by combining the deterministic nature of direct torque control and the adaptive nature of fuzzy logic control. Direct torque control using space vector pulse width modulation has been developed. This technique ensures the near-sinusoidal nature of the stator and rotor current. The impact of commutation ripple corresponding to the sinusoidal current is reduced compared to square wave current in conventional direct torque control. Further, the fuzzy logic controller provides adaptive modulation in space vector to mitigate the torque ripple. The response of the proposed method has been analyzed in the time domain as well as in the frequency domain. Experimental results establish a significant reduction in torque ripple and minimization of high-frequency components. A comparative study with conventional direct torque control methods has also been presented.

Keywords: Fuzzy logic controller, Direct torque controller, Harmonic analysis, PMBLDC drive, Space vector modulation techniques, Torque ripple, Discrete Fourier transform, Power spectrum density

Introduction

The modern transport and industrial sector are witnessing the ever-increasing application of permanent magnet brushless direct current (PMBLDC) motors as a main workhorse. PMBLDC motor has a major shortcoming of torque ripple. This restricts its application in vehicular field due to noise and vibrations [1]. Therefore, reducing the torque ripple has been the research focus over the last few decades. A fair amount of ongoing research is also concentrated in this field. The two major reasons for the torque ripple are the commutation of the phase currents and the non-ideal back-EMF waveform. In early literature, majority of torque ripple minimization methods are based on current shaping by injecting selected harmonic components in a phase current waveform [2]. These methods used complex Fourier decomposition and iterative approach to eliminate torque harmonics. The current harmonic injection technique

Karan *et al. Journal of Engineering and Applied Science* (2023) 70:66

Page 2 of 24

is based on open-loop cancellation concept which lacked experimental verification. There has been a consistent effort for reducing the commutation torque ripple with varying degrees of success. The torque ripple due to non-ideal back-EMF has also been addressed through creating an inverse of back-EMF waveform and assuming constant rotor speed [3–5]. In [6], the authors have established the effectiveness of suitable placement of space vectors for high DC bus voltage utilization. Significant reduction in total harmonic distortion has been experimentally verified with AC motor load. In [7], the authors have used space vector modulation with Dead-Beat direct torque control (DTC) and flux control strategy. A significant improvement is reported in a steady-state performance with the rapid dynamic response of the permanent magnet synchronous motor (PMSM) drive. However, the algorithm used has high computation complexity. In [8], the authors have used space vector pulse width modulation in conjunction with a duty-ratio regulator to synthesize the space vector. The variable duty-ratio achieves the desired reduction in torque ripple. This method reportedly achieves better steady-state performance with faster step response. In [9, 10], the authors have used fractional order-PID (FOPID) controller for speed control of a BLDC motor. The FOPID circuit has been realized by operational transconductance amplifiers (OTA) using an advanced circuit simulator. In [11, 12], the authors have addressed the torque ripple present in a PMBLDC motor drive. A Spider-based biologically inspired algorithm has been used to generate the pulse width modulated switching control. The torque ripple has been additionally addressed using a small dc-link capacitor with a single-phase voltage source. However, the torque ripple has been reportedly contained only up to 7%. In [13], the authors have used the differential evolution Krill-herd method, for optimization of controller gain in servo controller for BLDC motor. Although improvement in speed response has been established, the torque ripple mitigation has not been addressed. In [14–16], the authors have used the fuzzy logic control (FLC) to address the limitation of bandwidth of a PI control. The authors in [14] have used the adaptive FLC-based field weakening region of permanent magnet synchronous motor (PMSM) drive that gives it the better capability of field weakening and robust control. In [17], the authors have used FLC in a closed loop to overcome large phase delays in the estimation of back-emf. This method is used to extract the line-to-line back-EMF from the terminal voltage of a sensor-less BLDC motor drive. The fuzzy-based compensation in phase delay improves the commutation precision. In [18–20], FLC-based approach has been taken for the speed control of the BLDC motor. Here, the membership function has been tuned using an ANN-based algorithm. Simulation results show significant improvement in dynamic performance parameters. However, the negative torque ripple has not been addressed. In [21], the authors have used line to line flux linkage determination to achieve exact identification of rotor angle in a sensor-less BLDC motor. The accuracy of rotor angle estimation results in better implementation of mitigation process for commutation torque ripple. In [22], the authors have investigated the effect of sinusoidal phase current vis a vis square wave phase current in a PMBLDC motor and its effect on torque and torque ripple. Since sinusoidal current yields better result, it is better to use space vector pulse width modulation (SVPWM) which generates near sinusoidal phase current due to three level phase voltages applied to it. In this paper, the authors have

developed an adaptive space vector pulse width modulation based on fuzzy logic controller. The FLC has been developed based on error pattern shown in Fig. 1.

Methods

An adaptive space vector pulse width modulation based on fuzzy logic controller has been developed in order to mitigate torque ripples. Also, a comparative analysis with the two conventional Direct Torque Control methods has been done for validating the improvement in torque ripple of PMBLDC motor drive. The proposed methodology is explained using the block diagram in Fig. 2. The control strategy also has been shown using flow chart in Fig. 8. It has four major subsystems described as below:

Subsystem 1—flux and torque estimation

This subsystem estimates flux and torque in the PMBLDC motor. The Stator and rotor flux linkage as well as electromagnetic torque have been estimated using Eqs. (1)–(8).

The torque estimation for a PMBLDC motor with trapezoidal back-EMF is computed using (1) in stationary reference frame α-β.

$$T_e = \frac{3}{2}\frac{P}{2}\left[\frac{d\Psi_{r\alpha}}{d\theta_r}i_{s\alpha} + \frac{d\Psi_{r\beta}}{d\theta_r}i_{s\beta}\right] \tag{1}$$

where $\Psi_{r\alpha}$ and $\Psi_{r\beta}$ are the rotor flux linkage along α and β axis, respectively, θ_r is the rotor angle with respect to stator phase-A. P denotes the number of poles. $i_{s\alpha}, i_{s\beta}$ are stator current in stationary reference frame α-β.

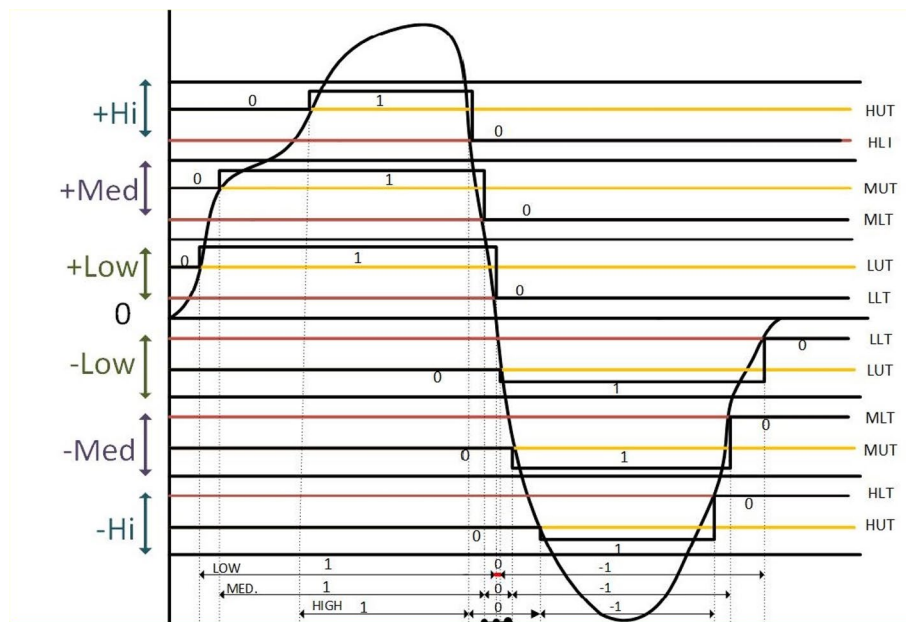The rotor flux linkages and angle can be obtained from the stator flux linkages by (2)–(4)

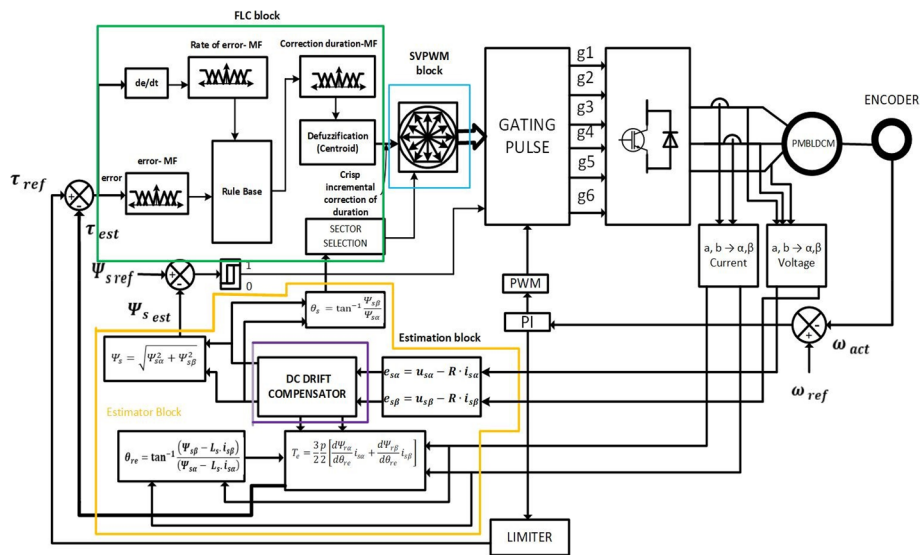**Fig. 1** Torque error analysis for proposed method

Fig. 2 Schematic block diagram of proposed method using fuzzy logic control

$$\Psi_{r\alpha} = \Psi_{s\alpha} - L_s.i_{s\alpha} \tag{2}$$

$$\Psi_{r\beta} = \Psi_{s\beta} - L_s.i_{s\beta} \tag{3}$$

$$\theta_r = \frac{\left(\Psi_{s\beta} - L_s.i_{s\beta}\right)}{\left(\Psi_{s\alpha} - L_s.i_{s\alpha}\right)} \tag{4}$$

where L_s is the inductance of the stator winding of a surface-mounted permanent magnet motor.

Stator flux linkage vector is expressed in terms of stator voltages $u_{s\alpha}, u_{s\beta}$, stator currents $i_{s\alpha}, i_{s\beta}$, and stator resistance R_s using (5) and (6). The magnitude (Ψ_s) and angular position (θ_s) of the stator flux linkage vector is obtained by (7)–(8).

$$\Psi_{s\alpha} = \int u_{s\alpha}.dt - R_s \int i_{s\alpha}.dt + \Psi_{s\alpha}(0) \tag{5}$$

$$\Psi_{s\beta} = \int u_{s\beta}.dt - R_s \int i_{s\beta}.dt + \Psi_{s\beta}(0) \tag{6}$$

$$\Psi_s = \sqrt{\Psi_{s\alpha}^2 + \Psi_{s\beta}^2} \tag{7}$$

$$\theta_s = \frac{\Psi_{s\beta}}{\Psi_{s\alpha}} \tag{8}$$

An analysis of shape of torque-error in a typical DTC control drive reveals a correlation between significant torque errors and rate of change in torque occurs. This error leads to a high torque ripple if not mitigated through equally fast corrective measures.

Karan *et al. Journal of Engineering and Applied Science*   (2023) 70:66

Page 5 of 24

Thus, there is a need to identify such control points and select an appropriate space vector to reduce the torque error with a befitting correction rate. In conventional DTC, this aspect is not taken care. Figure 1 shows the typical torque error pattern generated in a DTC. The error pattern has been categorized as low error, medium error, high error, and zero error. These different error ranges enable application of FLC in combination with the SVPWM technique for mitigation of torque ripple.

Subsystem 2—fuzzy logic controller

The FLC modulates the time duration of space vector for torque error correction depending on magnitude of torque error and rate of change of torque error. The working of FLC is explained below.

Generation of membership functions for FLC

The error and the rate of change of error between the reference torque and estimated torque have been divided into seven fuzzy membership functions. If the error is positive, then the positive error is assigned three membership functions viz. positive small (PS), positive medium (PM), and positive big (PB). However, if the error and rate of change of error are negative then they are assigned accordingly with other three membership functions viz. negative small (NS), negative medium (NM), and negative big (NB). The zero error is defined through membership fn. (Z) as shown in Fig. 3. The assignment of membership values corresponding to error values for any given membership function has been determined by an off-line ANN algorithm. The ANN algorithm is trained on the mathematical model of PMBLDC motor in order to minimize the torque error and the negative torque ripple. The developed membership functions for error, rate of change of error, and correction duration are shown by Fig. 3(a)–(c), respectively.

Fuzzy rule base

A fuzzy inference system (FIS) has been developed between the two input variables and one output variable. The input variables are error and rate of change of the error. The output variable is the incremental timing duration of space voltage vector. The output
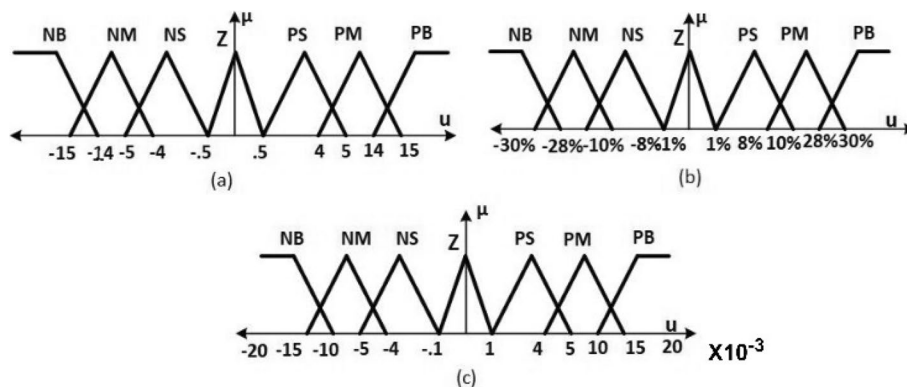

Fig. 3 **a** Torque error—membership function. **b** Rate of change of torque error-membership function. **c** Correction duration- membership function

Table 1 Rule base

		Rate of change of error: de/dt						
		NB	**NM**	**NS**	**ZE**	**PS**	**PM**	**PB**
Error: e	NB	NB	NB	NB	NM	NS	NS	ZE
	NM	NB	NM	NM	NM	NS	ZE	PS
	NS	NB	NM	NS	NS	ZE	PS	PB
	ZE	NB	NM	NS	ZE	PS	PM	PB
	PS	NM	NS	ZE	PS	PS	PM	PB
	PM	NS	ZE	PS	PM	PM	PM	PB
	PB	ZE	PS	PS	PM	PB	PB	PB
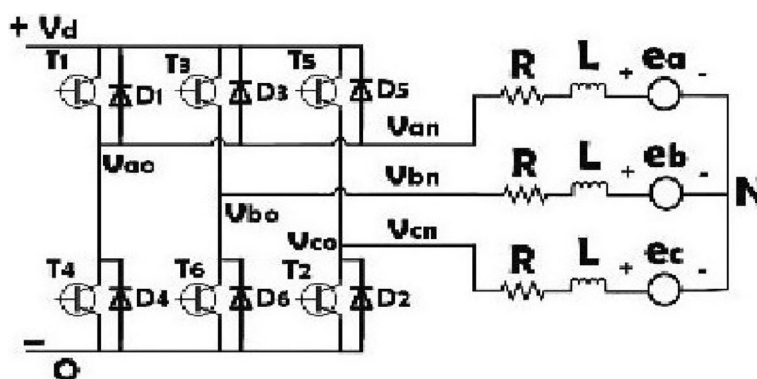
Fig. 4 VSI feeding PMBLDC motor

membership function is shown in Fig. 3(c). The rule base between input and output variables is represented by Table 1.

Generation of actuating signal

The FIS will select suitable membership function for implementing correction in time duration of a particular space vector. This is done by computing the centroid of output membership function. The centroid value represents the positive or negative incremental crisp value of time duration of the space voltage vector. The output variable for correction in time duration is given by the fuzzy logic control (FLC) system.

Subsystem 3—SVPWM control

To implement the torque control, the required space vector is synthesized by two adjacent vectors and null vector, by using SVPWM block. The three phase Voltage Source Inverter (VSI) feeding the PMBLDC motor is used for implementing the SVPWM technique. Three phase voltage source inverter and space vector diagrams are given in Figs. 4 and 5. In Fig. 5, the diagram shows the time duration of T1 and T2. T1 is the time for which vector V1 is applied, and T2 is the time for which vector V2 is applied, and T0 is the time for which null vector is applied. T1, T2, T0, and modulation index *a* are calculated in SVPWM block using (9)-(12).
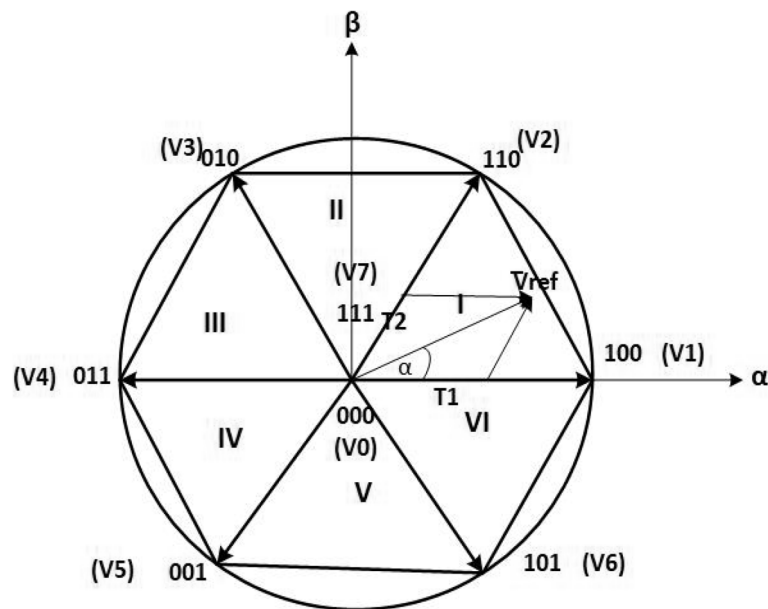
Fig. 5 Space vector diagram for SVPWM

$$T_1 = \frac{\sqrt{3}}{V_{dc}} T_z * \left| \overrightarrow{V}_{ref} \right| * \left[\sin\left(n * \frac{\pi}{3} - \alpha \right) \right] \tag{9}$$

$$T_2 = \frac{\sqrt{3}}{V_{dc}} T_z * \left| \overrightarrow{V}_{ref} \right| * \left[\sin\left(\alpha - \frac{n-1}{3} * \pi \right) \right] \tag{10}$$

$$T_0 = T_z - (T_1 + T_2) \tag{11}$$

$$a = \frac{\left| \overrightarrow{V}_{ref} \right|}{\frac{2}{3} * V_{dc}} \tag{12}$$

Here, a is the modulation index, n is the number of sectors, and T_z is the sampling time. SVPWM switching sequence showing the status of the upper and lower switching transistors are shown by diagram in Fig. 6, for sector 1 and sector 2. Effect of modulation in switching time duration on the resultant voltage vector in case of sector 1 is shown below in Fig. 7(a)–(c) under three possible scenarios.

Scenario 1

When the correction in time duration is within the zero-membership zone, the output of FLC will have zero incremental value as crisp value. The addition of this value to the T1 or T2 will have no change in space voltage vector as shown in Fig. 7(a).

Scenario 2

When the correction in time duration has positive incremental value as output of FLC, the incremental crisp value is added to the time duration of the leading space voltage
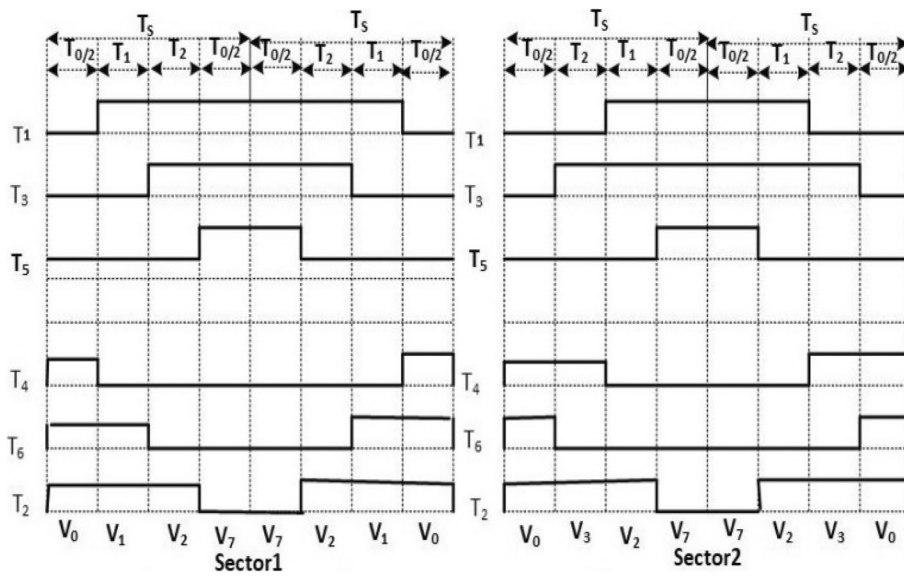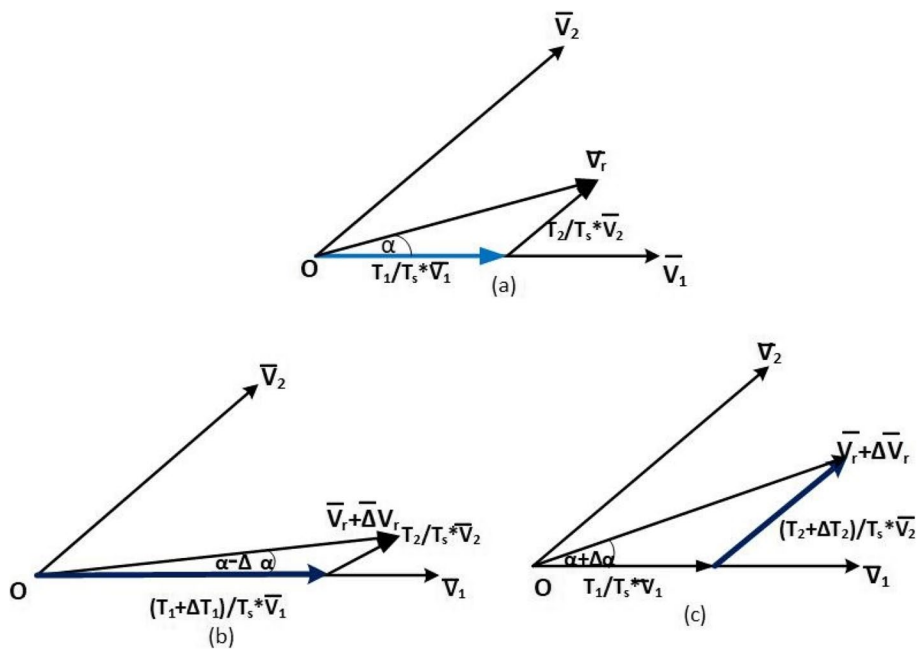
Fig. 6 SVPWM switching sequence for sector1 and sector 2

Fig. 7 a No change, **b** decrease in torque, and **c** increase in torque

vector. This results in the incremental increase in the magnitude of the resultant space vector V_r in the direction of rotation to correct the desired torque as shown in the Fig. 7(b).

Scenario 3

When the correction in time duration has negative incremental value as output of FLC, the magnitude of incremental crisp value is added to the time duration of the lagging

Karan *et al. Journal of Engineering and Applied Science* (2023) 70:66

Page 9 of 24

space voltage vector. This results in the incremental increase in the magnitude of the resultant space vector V_r in the opposite direction of rotation to correct the desired torque as shown in Fig. 7 (c). The proposed method has been validated through simulation and experimental work.

Subsystem 4—DC drift compensation

The DC drift compensation block uses adaptive magnitude compensation (AMC) for elimination of DC offset in stator flux linkage [23]. The proposed method addresses the problem of pure integration-related dc drift and eliminates DC offset in stator flux linkage. Adaptive magnitude compensation compares two components, feed forward and feedback, one from the output of the (LPF) low pass filter and second from the output of the magnitude compensation feedback, till the error is zero at the point of back-emf and flux becoming orthogonal to each other. The result is shown in Fig. 16, with the x–y plot of Psi-alpha and Psi-beta. The plot shows the effect of AMC in the final output of flux magnitude, which after transient, migrates to zero DC offset in the steady state. The proposed control strategy has been shown using flow chart in Fig. 8. This illustrates mechanism for fuzzy logic-based space vector modulation depending upon torque error. This has been explained in previous section in detail.
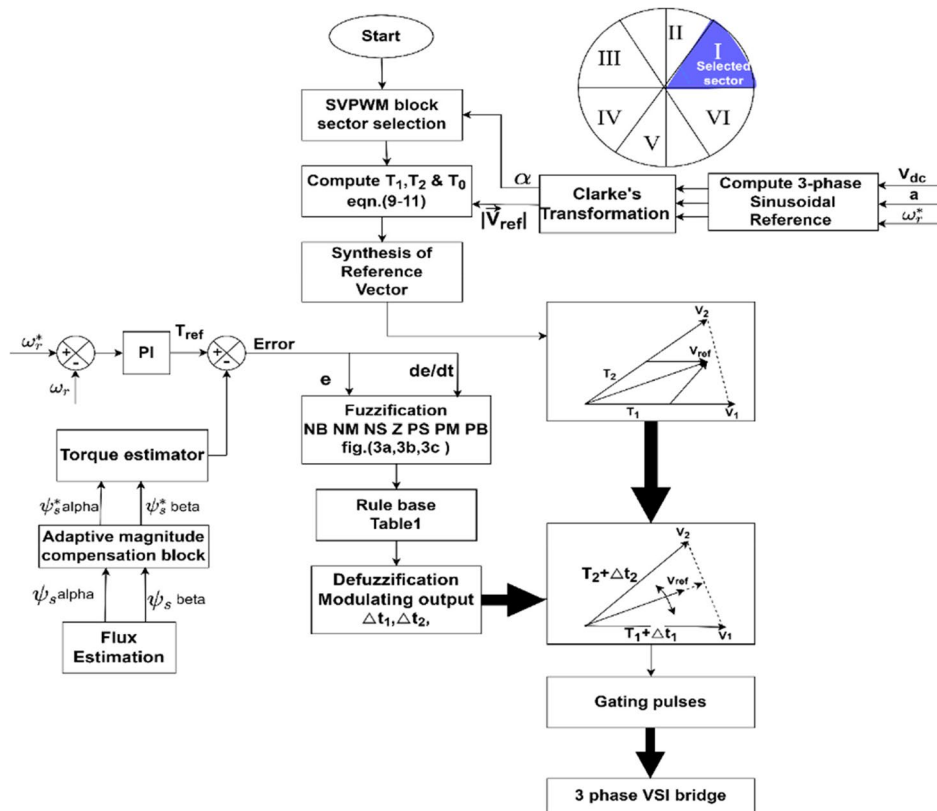

Fig. 8 The flow chart for proposed methodology

A comparative study of conventional DTC and SVPWM and FLC-based adaptive DTC

A conventional DTC scheme uses square wave current, whereas a SVPWM-based DTC scheme employs a three-level phase voltage to produce near sinusoidal wave current. Investigation of simulation result Fig. 16 and experimental result corresponding Fig. 26 shows the better performance of the sinusoidal current supply both from the point of view of the motor torque and the torque ripple. The torque ripple with sinusoidal current supply is constant from zero up to the base speed, while it changes with the speed during the commutations for the square-wave current supply in case of conventional DTC. This is due to the phase inductance of the motor which slows down both rise and fall of the phase currents in case of square wave currents. Figure 9 below explains the commutation ripple in conventional DTC as a result of unequal rate of falling and rising currents due to phase inductances. At lower speed, the torque ripple is positive, and at higher speed, it is negative. The torque ripple with sinusoidal current supply is much lower both at low and high speed.

A conventional DTC applies a single-voltage vector to correct torque error. This produces fixed torque irrespective of the magnitude of torque error. Thus, causing overshoot. Whereas in fuzzy logic-based DTC, the magnitude of torque error as well as the rate of change of error has been divided under seven membership functions to
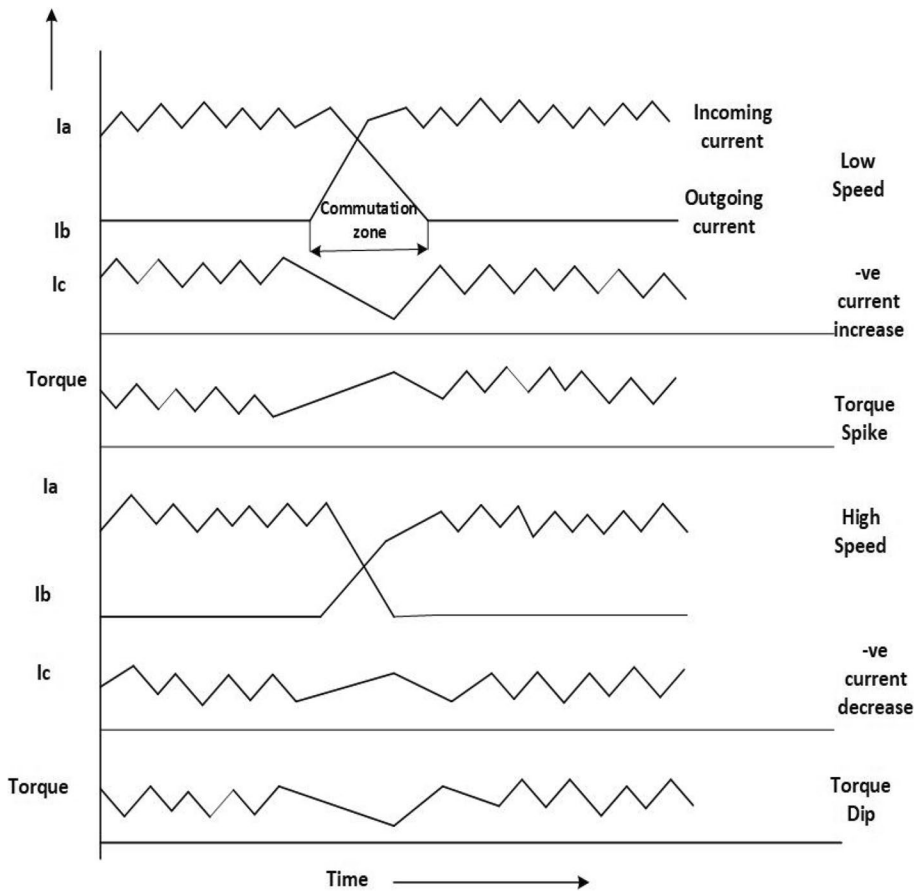

Fig. 9 Analysis of commutation torque ripple in conventional DTC

limit the over shoot of error correction. This mechanism is shown using flowchart in Fig. 8. A comparative result of torque ripple has been presented in Tables 2 and 3 as compared to other evolutionary algorithms [20]. Table 4 shows a comparison of the proposed method with conventional DTC methods in terms of percentage torque ripple for a wide-speed range (20 to 100 rad/s). However, at a very low speed, flux and torque estimation becomes very difficult due to negligible back EMF. The literature on neural network based PMBLDC drives is limited.

Table 2 Motor parameter

Numbers of poles, *p*	8
DC link voltage (V)	96
Rated speed (rpm)	1000
Motor power (kW)	1.0
Flux Linkage (Weber)	0.0396
Stator phase resistance (ohm)	.035
Stator inductance (mH)	.075
Torque constant (Nm/Apk)	0.6336
Voltage constant(V/k-RPM)	66.53
Damping constant (Nm-s)	.000305
Motor inertia (kg-m^2)	.00062

Table 3 Proposed method torque ripple percent at various speeds compared to various other methods

Speed (rad/s)	Torque ripple percentage achieved through various other methods						Proposed method
	BA (Bat Algo.)	PSO (particle swarm optimization)	ALO (Ant Lion Optimizer)	Integrated Dual DC-DC output Conv	GA (Genetic Algo.- based control.)	ANFIS + Fire Fly Algo. control	
30	8.02%	8.67%	7.25%	11.4%	-	5.98%	2.89%
40	-	-	-	-	-	-	2.33%
50	15.2%	17.1%	10.3%	-	-	8.795	1.27%
60	-	-	-	-	-	-	1.06%
70	13.7%	13.98%	11.5%	-	-	9.1%	4.56%
80	-	-	-	-	-	-	5.43%
100	14.8%	16.7%	14.0%	16.2%	12.2%	10.5%	5.6%

Table 4 Torque ripple percent comparison

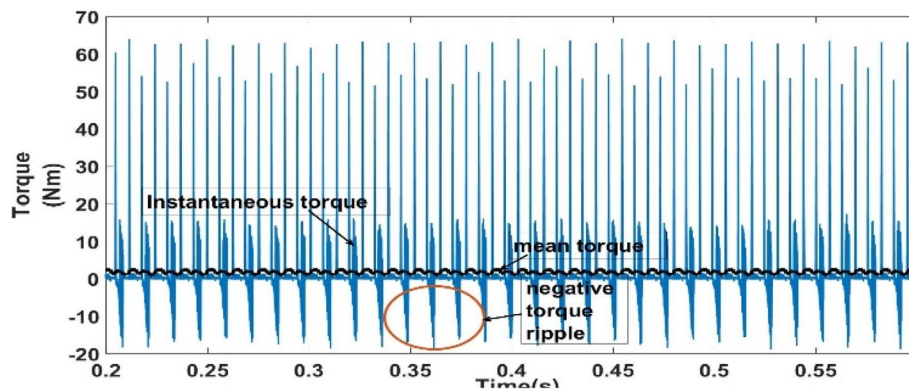| Speed (rad/s)	DTC method 1	DTC method 2	DTC-FLC
20	93%	50.6%	10.2%
40	66.7%	21.9%	2.33%
60	44%	14.1%	5.01%
80	73%	14.7%	3.36%
100	47.6%	28.9%	5.6%

Fig. 10 Method 1—instantaneous and mean torque value
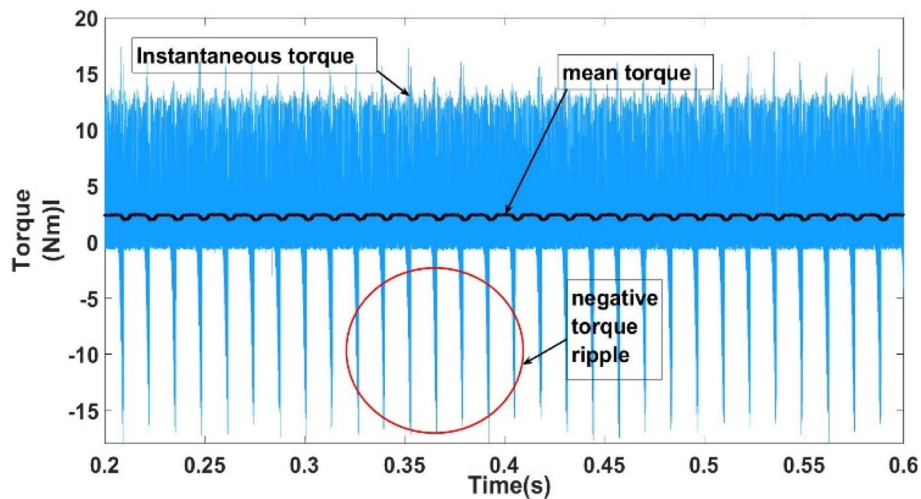

Fig. 11 Method 2—instantaneous and mean torque value

Results and discussions

The simulation and experimental results are discussed in the following subsections for validation of the proposed method. The comparative study of results of conventional DTC and proposed FLC-based SVPWM system have been analyzed both in time and frequency domain.

The simulation and experiment have been conducted on eight pole PM BLDC motor with the following parameters given in the Table 2. The load torque was provided using a coupled DC generator with electrical loading.

Simulation results and discussions

The developed model was simulated with the PMBLDC motor with the parameter given in Table 2, at a load torque of 10 N-m and at a speed of 40 rad/s. For comparative study, two other conventional DTC methods are also simulated. Here, method 1 uses six space voltage vectors and two-phase switching DTC and method 2 uses six space voltage vectors with three-phase switching DTC. The results of simulations presenting instantaneous and mean
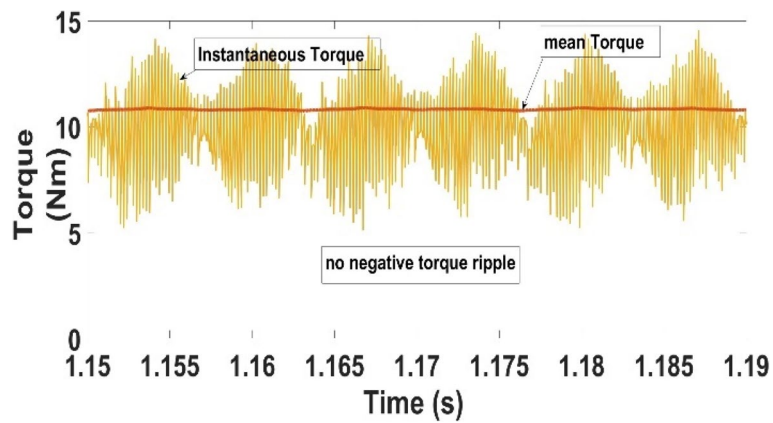
Fig. 12 Proposed method—instantaneous and mean torque value

torque value are shown in Figs. 10, 11, and 12. The torque ripple in case of all three methods has been computed using (13). The mean torque in each case has been zoomed and shown in Figs. 13, 14, and 15, where the proposed method shows significant improvement (2.33%) in torque ripple shown in Fig. 15, as compared to other two conventional DTC methods. To further validate proposed method, the simulation was run from 20 to 100 rad/s speed with an incremental step of 20 rad/s. Figure 16 shows the simulation results of the proposed method at 40, 60, 80, and 100 rad/s of varying speed command. The comparative results of torque ripple have been tabulated in Table 4. The proposed method shows better torque ripple mitigation for a wide-speed range.

$$T_{-ripple}\% = \frac{T_{max} - T_{min}}{T_{avg}} \times 100 \tag{13}$$
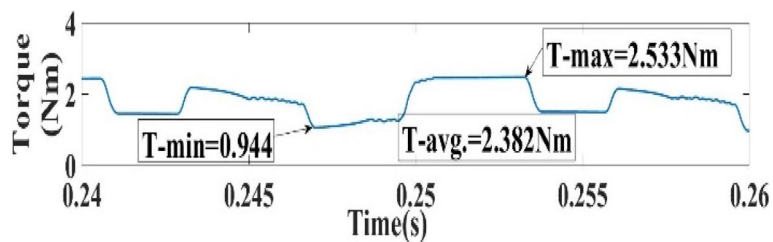
Fig. 13 Method 1—torque ripple (66.7%)
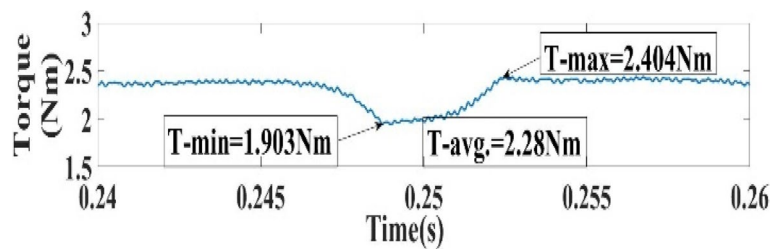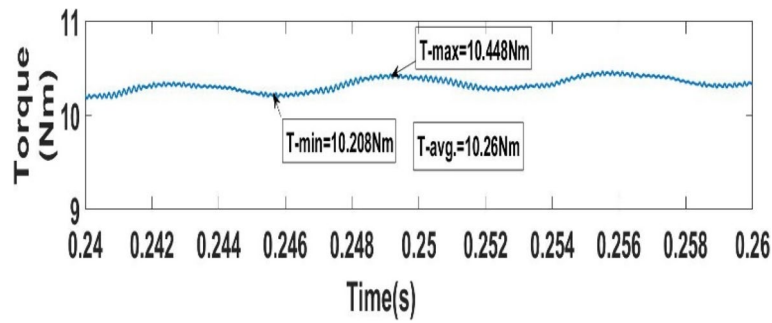

Fig. 14 Method 2—torque ripple (21.97%)

Fig. 15 Proposed method—torque ripple (2.33%)
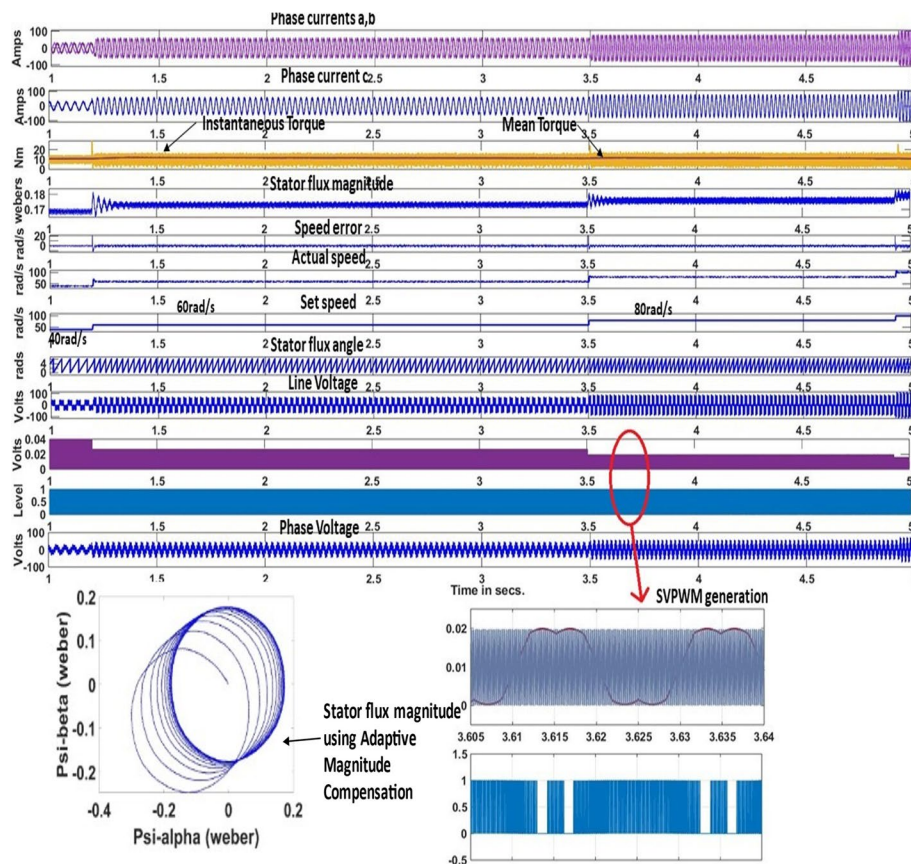

Fig. 16 Proposed method simulation for 10Nm with varying speeds of motor at 40 rad/s, 69 rad/s, 80 rad/s, and 100 rad/s showing respective stator phase currents, torques, stator flux magnitudes, angles, speed error actual speeds, and set speed with line and phase voltage

Step response and frequency response analysis

Step response

The speed response obtained from simulation is shown in Fig. 16 for various speed commands. Further, the transient characteristics corresponding to speed command of 40 rad/s, 60 rad/s, and 80 rad/s have been zoomed in and shown Figs. 17, 18, and 19,
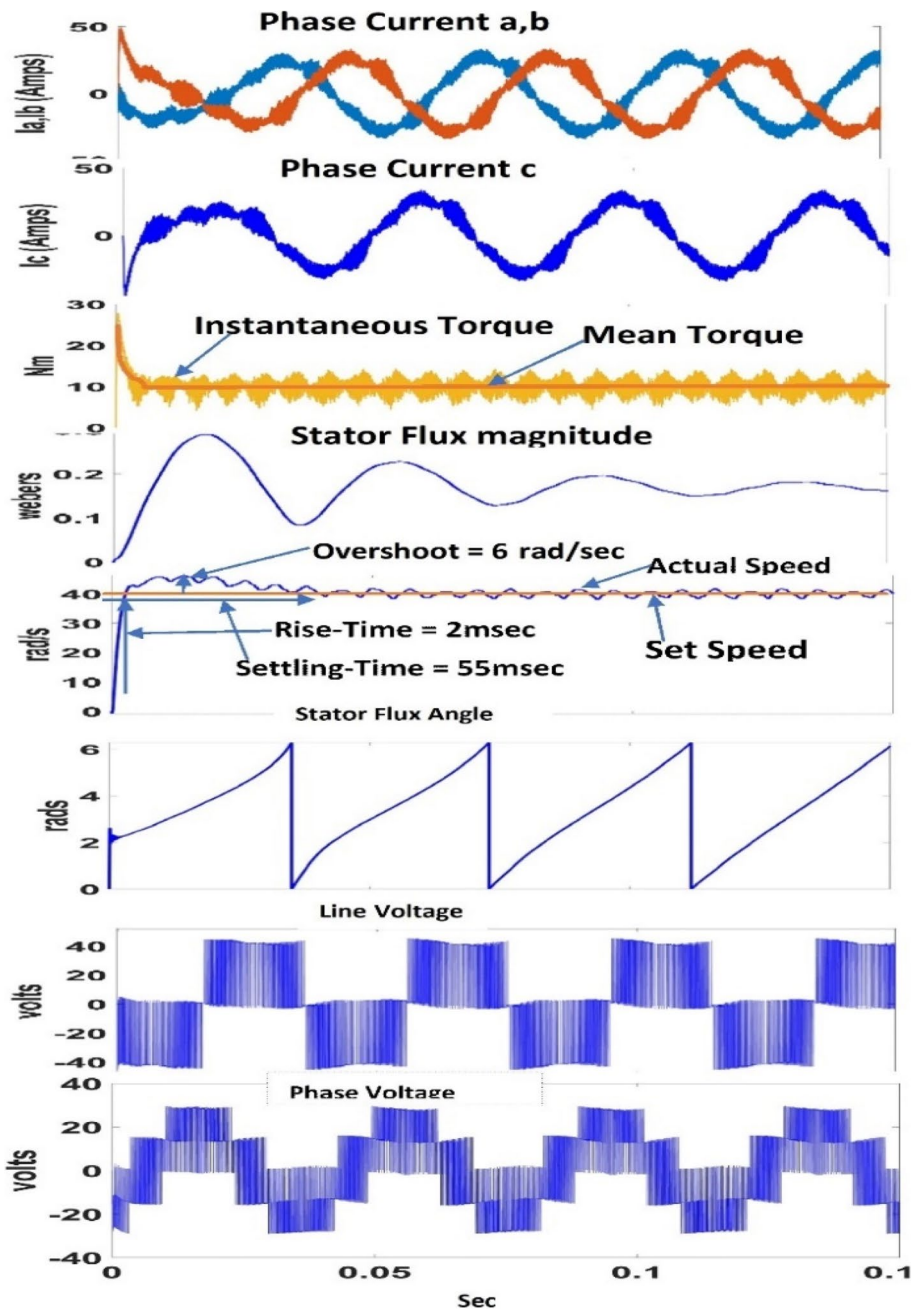
Karan *et al. Journal of Engineering and Applied Science*   (2023) 70:66

Page 15 of 24

Fig. 17 Transient and steady-state response captured at step 1 (0–40 rad/s) and 10-Nm load torque for the proposed method

respectively. Dynamic parameters of time domain response for different speed-step command are given in Table 5.

Frequency response

The frequency response of torque dynamics of the proposed method has been computed from real-time data and presented in Fig. 20. Also, frequency responses of method 1 and method 2 has been compared over the wide frequency range. The harmonic content of
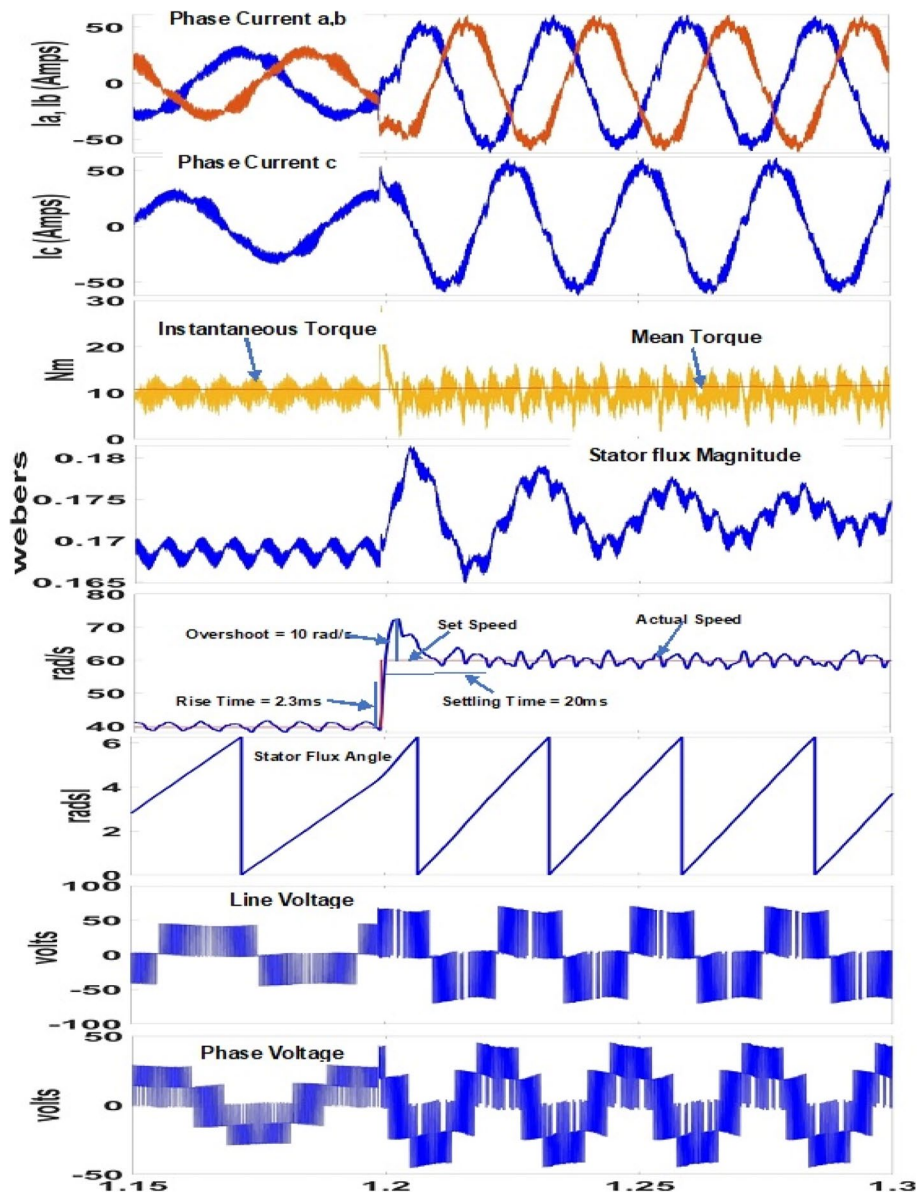
Fig. 18 Transient and steady-state response captured at step 2 (40 to 60 rad/s) at 10-Nm load torque for the proposed method

torque ripple has been obtained by performing discrete Fourier transform (DFT) on torque data using (14). Further, the obtained harmonic content has been used to compute power spectrum density (PSD) of the frequency spectrum of torque data using Eq. (15).

$$X(K) = \sum_{n=0}^{N-1} X(n).e^{-\frac{j2\pi Kn}{N}} \qquad (14)$$

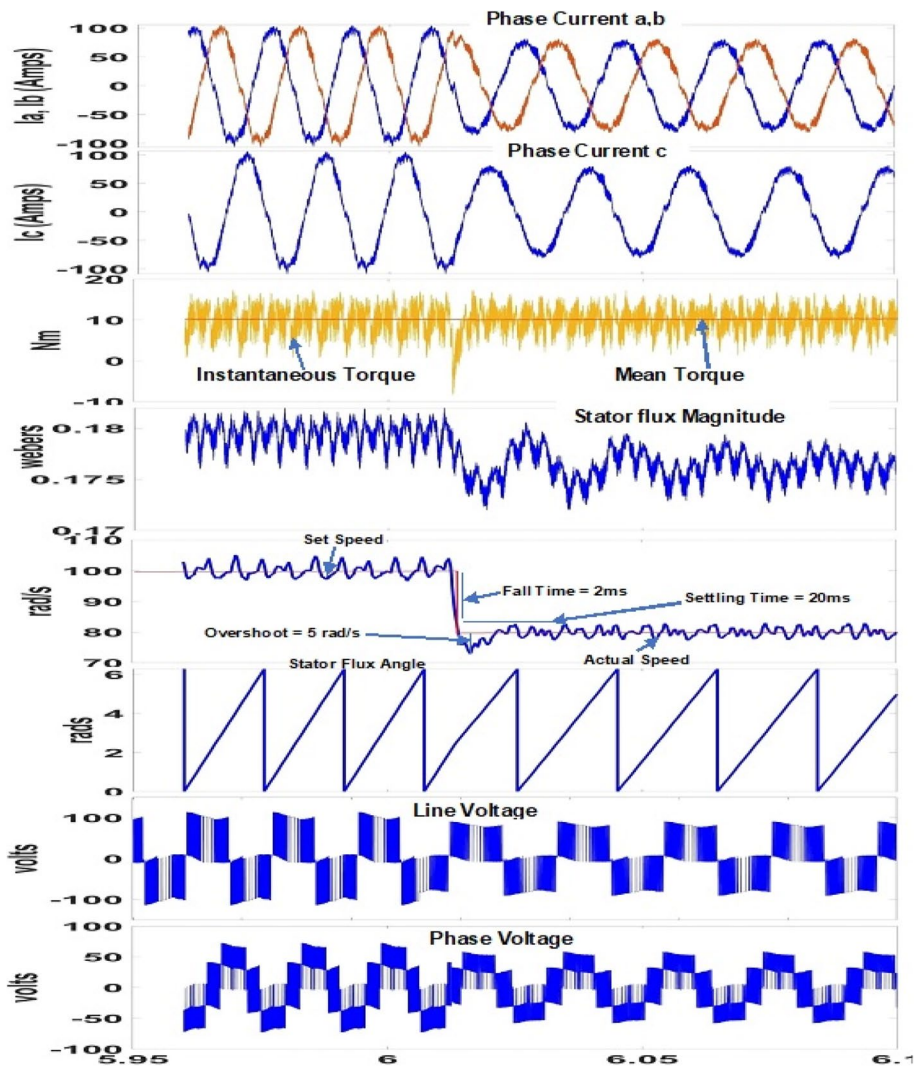$$PSD = \frac{1}{N} \sum_{K=0}^{N-1} (X(K))^2 \qquad (15)$$

Fig. 19 Transient and steady-state response captured at step 3 (100 to 80 rad/s) at 10-Nm load torque for the proposed method

Table 5 Step response of the proposed methodology

	Step changes	Rise/fall time	% Overshoot	Settling time
Step 1	0–40 rad/s	2 ms	15	55 ms
Step 2	40–60 rad/s	2 ms	16.6	20 ms
Step 3	100–80 rad/s	2 ms	6.25	20 ms

where $K=1,2, 3\ N\text{-}1$, is the order of harmonics; $n=1,2, 3\ N\text{-}1$, is the no. of samples; $N=$ total no. of samples.

$X(K)$ represents the frequency component of the observed signal, and K is the number of harmonics. $X(K)$ for method 1 and method 2 and the proposed method has been shown in Fig. 20. The proposed method represented shows low lower order harmonic
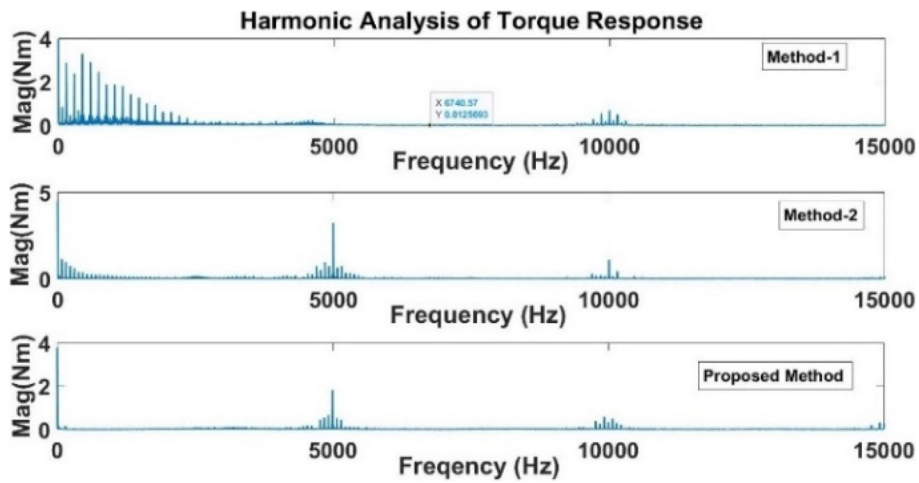
Karan *et al. Journal of Engineering and Applied Science*   (2023) 70:66

Page 18 of 24

Fig. 20 Frequency-spectrum of torque for method 1, method 2, and the proposed method torque for 2Nm, 40 rad/s
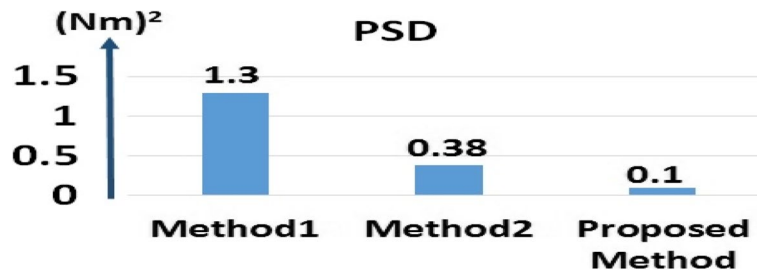

Fig. 21 Power spectrum density of amplitude of torque for method 1, method 2, and proposed method

content. A comparative picture of PSD obtained from torque amplitudes is shown in Fig. 21. The proposed method shows a considerable reduction in the PSD value implying overall torque ripple reduction.

The statistical analysis of performance indices is done using integral absolute error (IAE), integral square error (ISE), integral time-weighted square error (ITSE), and integral time-weighted absolute error (ITAE) using Eqs. (16)–(19).

$$IAE = \int_0^\infty |e(t)| dt \tag{16}$$

$$ISE = \int_0^\infty e(t)^2 dt \tag{17}$$

$$ISTE = \int_0^\infty t * e(t)^2 dt \tag{18}$$

$$IATE = \int_0^\infty t * |e(t)| dt \tag{19}$$

Table 6 Performance indices of speed and torque response

	Speed error			Torque error		
	DTC method 1	DTC method 2	DTC-FLC	DTC method 1	DTC method 2	DTC-FLC
IAE	0.82	0.243	0.1567	0.1968	0.105	0.0568
ISE	10.1	8.195	5.169	0.2766	0.22	0.1746
ISTE	0.18	0.02973	0.00895	0.0161	0.001	0.00005
IATE	0.015	0.0011	0.0008	0.013	0.011	0.00146

Fig. 22 Experimental set-up for validating simulation results for all methods

The computed performance indices for speed response and torque response are given in Table 6.

The proposed method shows better performance in terms of lower values of statistical performance indices as compared to other methods.

Experimental results and discussions

Experimental setup has been developed to verify the simulation results of the proposed method. The set-up is shown in Fig. 22. The system is based on RT1104 /d-SPACE. The schematic diagram of the experimental set-up has been given in Fig. 23, in order to elaborate the d-SPACE based real-time control.

The three-phase voltage, current, and motor speed are fed back with the help of ADC channels. The gating signals are obtained through the digital I/O board of dSPACE. The 1-kW PMBLDC motor has been taken for the experiment. It is coupled to a separately excited DC generator with the provision of electrical loading. All the control techniques have been implemented at step time 50 μ-seconds. This sampling time has been selected on account of minimum possible sampling time supported by the real-time simulator (dSPACE 1104) for real-time implementation of the proposed method. DC generator voltage is taken as actual speed of motor. The HX-20P Hall effect current transducers and the LV-25P voltage transducer are used to measure phase currents and line voltages, respectively. The experimental results are presented in Figs. 24, 25, and 26 corresponding to method 1, method 2, and proposed method. Figure 24 shows a large negative torque ripple marked by red circle. A
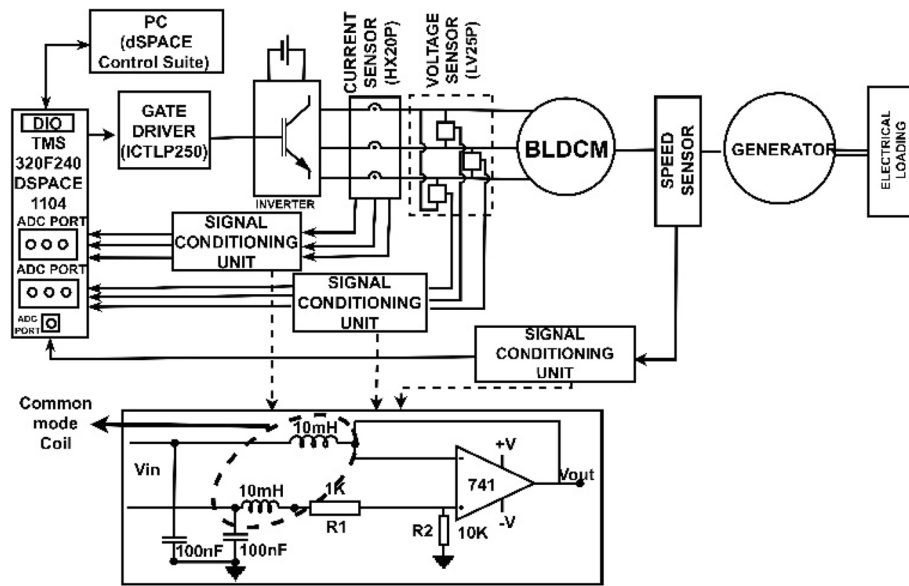
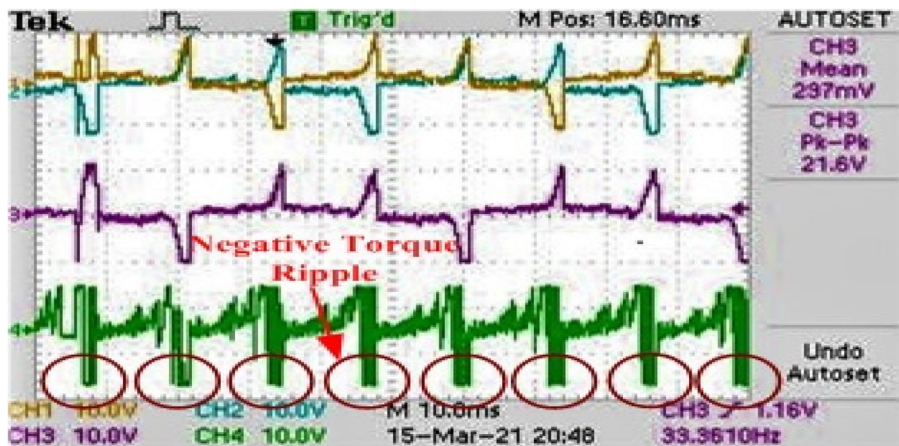**Fig. 23** Schematic diagram of experimental set-up

Fig. 24 Results of conventional method 1 for 2Nm, 40 rads/s. Current scale: 1 V = 2 Amp, Torque scale: 1 V = 4 Nm, T-avg. = 2.38Nm

slightly improved negative torque ripple is observed in Fig. 25. The result of proposed method shows no negative torque ripple as shown in Fig. 26.

The Table 3 represents work of other papers [20], in which computational burden has not been discussed. However, the computational burden of proposed work has been obtained in terms of maximum memory allocation and maximum number of clock cycles. The maximum memory allocated on the DSPACE 1104 processor is 110 K Bytes, and number of clock cycles is $2.22 * 10^3$. The clock frequency is 40 MHz. The other algorithms in Table 3 are evolutionary in nature that require multiple time (k-times) computation of objective function for multiple N-operating points in a single iteration. This makes the complexity of higher order expressed as big-O notation
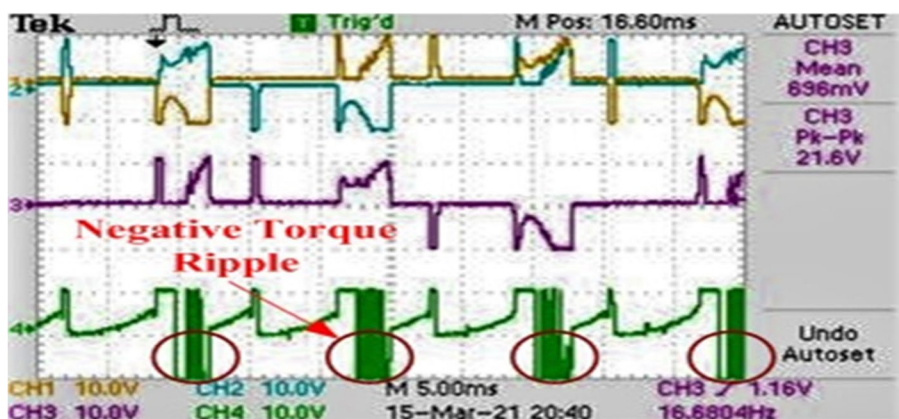
Fig. 25 Results of conventional method 2 for 2 Nm, 40 rads/s. Current scale: 1 V = 2 Amp, torque scale: 1 V = 4 Nm, T- avg. = 2.28Nm
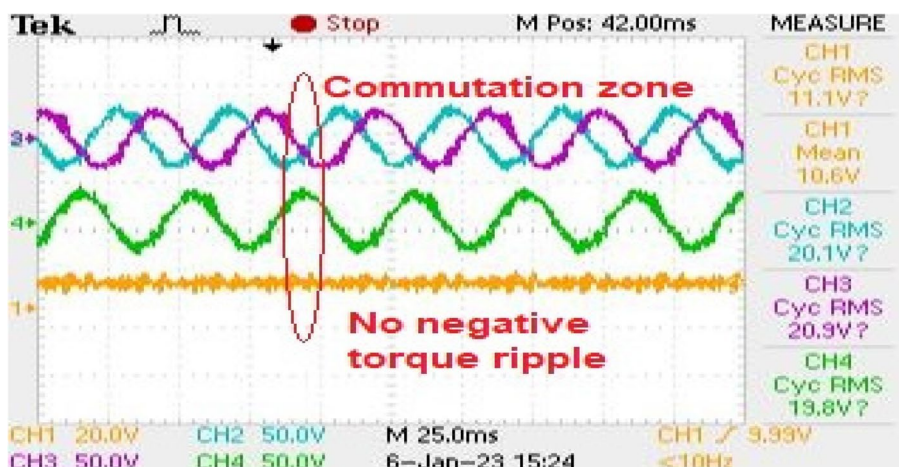

Fig. 26 Results of proposed method for 10Nm, 40 rads/s. Current scale:1 V = 10 Amp, torque scale: 1 V = 1 Nm, T-avg. = 10.6Nm

in order of O (N^k). The proposed algorithm has linear complexity as there is no computation for multiple generations or operating points in a single loop expressed as O (N).

The time dynamic parameters of simulation results as shown in Fig. 17 and that of experimental results shown in 30 and 31 have been compared in Table 7 (Figs. 27 and 28).

Conclusions

This paper presents a modified DTC technique for torque ripple reduction by combining advantages of SVPWM with adaptive nature of FLC. SVPWM-based DTC provides near sinusoidal phase current response as compared to square wave phase current of conventional DTC. This results in sinusoidal nature of commutating current with equal rate of rise and rate of fall at wide range of speed. This mitigates torque ripple to a great extent that is caused due to square wave nature of the commutating phase current. However, in SVPWM-based DTC, the bounding space vectors corresponding to a particular sector are

Table 7 Detailed comparison between simulation and experimental results

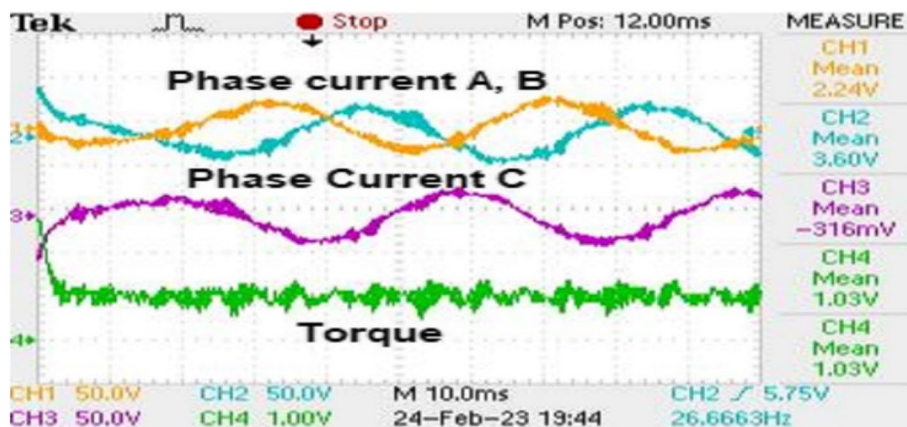|	Step changes	Rise time	Overshoot	Settling time	Mean torque	Negative torque ripple	Percent torque ripple
Simulation results	Start point to 40 rad/s	2.0 ms	6 rad/s	55 ms	10.2Nm	Nil	2.33
Experiment results	Start point to 40 rad/s	2.4 ms	10.5 rad/s	60 ms	10.3Nm	Nil	2.4

Fig. 27 Results of proposed method for 10Nm, 40 rads/s. Current scale: 1 V = 10 Amp, torque scale: 1 V = 1 Nm, T-avg. = 10.3Nm
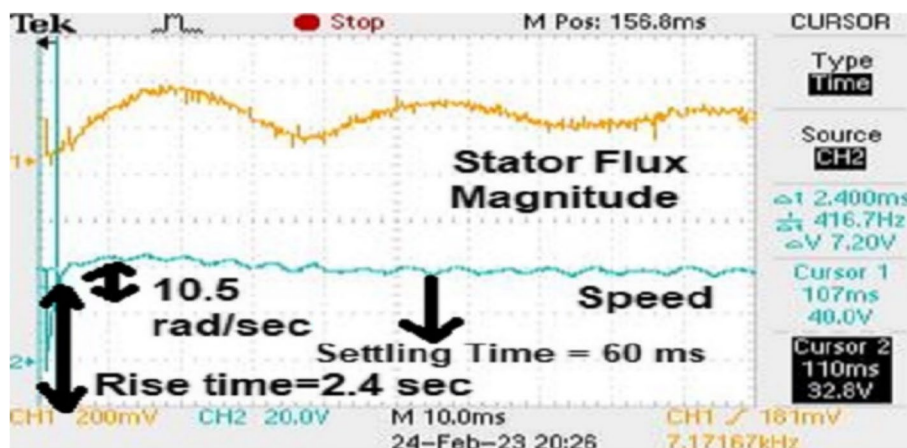

Fig. 28 Results of proposed method for 10Nm, 40 rads/s. Stator flux magnitude scale: 1 milli volt = 0.77 milli weber, actual speed scale: 1 V = 1 rad/s

selected according to the position of flux vector. The duration of bounding space vectors cannot be modulated. This feature is added by FLC. The FLC-based SVPWM-DTC modulates the space vector according to error and rate of change of error by categorizing them in seven membership functions. The proposed method is analyzed using simulation and validated through experimental data. A comparative analysis between conventional DTC and the proposed method establishes significant improvement in mitigation of torque ripple.

Abbreviations

PMBLDC	Permanent magnet brushless DC motor
FOPID	Fractional order proportional integral differential control
DTC	Direct torque control
VSI	Voltage source inverter
EMF	Electro motive force
PWM	Pulse width modulation
DC	Direct current
LPF	Low pass filter
PI	Proportional integral control
ST-DTC	Switching table-based direct torque control
SVM-DTC	Space vector modulation-based direct torque control
BLDC	Brushless DC motor
DFT	Discrete Fourier transform
PSD	Power spectrum density
OTA	Operational transconductan amplifiers
FLC	Fuzzy logic control
SVPWM	Space vector pulse width modulation
ANN	Adaptive neural network
PMSM	Permanent magnet synchronous motor
IAE	Integral absolute error
ISE	Integral square error
ITSE	Integral time-weighted square error
ITAE	Integral time-weighted absolute error
BA	Bat Algorithm
FF	Fire fly algorithm
ANFIS	Adaptive neuro fuzzy inference system
ALO	Ant lion algorithm
PSO	Particle swarm algorithm
GA	Genetic algorithm
AMC	Adaptive Magnitude compensation
FIS	Fuzzy inference system
NS	Negative small
NM	Negative medium
NB	Negative big
Z	Zero
PS	Positive small
PM	Positive medium
PB	Positive big

Availability of data and materials

All data generated or analyzed during this study are included in this published article.

Declarations

Competing interests

The authors declare that they have no competing interests.

References

1. Chan CC (1993) An overview of electric vehicle technology. Proc IEEE 81(9):1202–1213. https://doi.org/10.1109/5.237530
2. Hung JY, Ding Z (1993) Design of currents to reduce torque ripple in brushless permanent magnet motors. IEE Proc B Electr Power Appl 140(4):260–266. https://doi.org/10.1049/ip-b.1993.0032

Karan *et al. Journal of Engineering and Applied Science*   (2023) 70:66

Page 24 of 24

3.   Zhu ZQ, Liu Y, Howe D (2005) Comparison of performance of brushless DC drives under direct torque control and PWM current control. 2005 Int Conf Electr Mach Syst 2(1):1486–1491. https://doi.org/10.1109/ICEMS.2005.202797

4.   Tan H (2001) Controllability analysis of torque ripple due to phase commutation in brushless DC motors. ICEMS 2001 Proc. 5th Int Conf Electr Mach Syst 2:1317–1322. https://doi.org/10.1109/ICEMS.2001.971926

5.   Kawase Y, Murai Y et al (1989) Torque ripple improvement for brushless DC miniature motors. IEEE Trans Ind Appl 25(3):441–450. https://doi.org/10.1109/28.31214

6.   Huang Z, Yang T, Giangrande P, Chowdhury S, Galea M, Wheeler P (2021) Enhanced performance of dual inverter with a floating capacitor for motor drive applications. IEEE Trans Power Electron 36(6):6903–6916. https://doi.org/10.1109/TPEL.2020.3040029

7.   Lin X, Huang W, Jiang W, Zhao Y, Zhu S (2020) Deadbeat direct torque and flux control for permanent magnet synchronous motor based on stator flux oriented. IEEE Trans Power Electron 35(5):5078–5092. https://doi.org/10.1109/TPEL.2019.2946738

8.   Adase LA, Alsofyani IM, Lee KB (2020) Predictive torque control with simple duty-ratio regulator of PMSM for minimizing torque and flux ripples. IEEE Access 8:2373–2381. https://doi.org/10.1109/ACCESS.2019.2961935

9.   George MA, Kamat DV, Indiran T (2021) OTA-C realization of an optimized FOPID controller for BLDC motor speed control. IETE J Res. https://doi.org/10.1080/03772063.2021.1951380

10. Mohammed Eltoum MA, Hussein A, Abido MA (2021) Hybrid fuzzy fractional-order PID-based speed control for brushless DC motor. Arab J Sci Eng. 46(10):9423–9435. https://doi.org/10.1007/s13369-020-05262-3

11. Maharajan MP, Xavier SAE (2019) Design of speed control and reduction of torque ripple factor in BLdc motor using spider based controller. IEEE Trans Power Electron 34(8):7826–7837. https://doi.org/10.1109/TPEL.2018.2880916

12. A. Fathima, Vijayasree G. Design of BLDC motor with torque ripple reduction using spider-based controller for both sensored and sensorless approach, Arab. J. Sci. Eng., no. 0123456789 2021 https://doi.org/10.1007/s13369-021-05833-y.

13. Alex SS, Daniel AE (2020) Optimal gain selection strategy in back EMF observer for position sensorless operation of BLDC motors. Arab J Sci Eng 45(3):1345–1356. https://doi.org/10.1007/s13369-019-03908-5

14. Wang C, Zhu ZQ (2020) Fuzzy logic speed control of permanent magnet synchronous machine and feedback voltage ripple reduction in flux-weakening operation region. IEEE Trans Ind Appl 56(2):1505–1517. https://doi.org/10.1109/TIA.2020.2967673

15. Tang L, Han Z, Xu Z (2021) A sequential adaptive control strategy for the contact colliding speed of contactors based on fuzzy control. IEEE Trans Ind Electron 68(7):6064–6074. https://doi.org/10.1109/TIE.2020.2994872

16. N. Farah, M. H. N. Talib, Z. Ibrahim, S. N. M. Isa, and J. M. Lazi, Variable hysteresis current controller with fuzzy logic controller based induction motor drives, 2017 7th IEEE Int. Conf. Syst. Eng. Technol. ICSET 2017 122–127, 2017. https://doi.org/10.1109/ICSEngT.2017.8123432.

17. Soni UK, Tripathi RK (2021) Sensorless control of high-speed BLDC motor using equal area criterion based precise commutation scheme with Fuzzy based phase delay compensation. Int Trans Electr Energy Syst 31(9):1–30. https://doi.org/10.1002/2050-7038.13001

18. Ramya A, Balaji M, Kamaraj V (2019) Adaptive MF tuned fuzzy logic speed controller for BLDC motor drive using ANN and PSO technique. J Eng 2019(17):3947–3950. https://doi.org/10.1049/joe.2018.8179

19. Sankardoss V, Geethanjali P (2021) Design and low-cost implementation of an electric wheelchair control. IETE J Res 67(5):657–666. https://doi.org/10.1080/03772063.2019.1565951

20. Prathibanandhi K, Ramesh R (2018) Hybrid control technique for minimizing the torque ripple of brushless direct current motor. Meas Control (United Kingdom) 51(7–8):321–335. https://doi.org/10.1177/0020294018786753

21. Jafarboland M, Silabi MHR (2019) New sensorless commutation method for BLDC motors based on the line-to-line flux linkage theory. IET Electr Power Appl 13(6):757–765. https://doi.org/10.1049/iet-epa.2018.5356

22. Bertoluzzo M, Buja G, Keshri RK, Menis R (2015) Sinusoidal versus square-wave current supply of PM brushless DC drives: a convenience analysis. IEEE Trans Ind Electron 62(12):7339–7349. https://doi.org/10.1109/TIE.2015.2455518

23. Hu J, Wu B (1998) New integration algorithms for estimating motor flux over a wide speed range. IEEE Trans Power Electron 13(5):969–977. https://doi.org/10.1109/63.712323

Publisher's Note